Prescribed Grass Fire Mapping and Rate of Spread Measurement Using NIR Images from a Small Fixed-Wing UAS

Saket Gowravaram, Haiyang Chao, Zhenghao Lin, Sheena Parsons, Tiebiao Zhao, Ming Xin, Xiaolin Hu, Pengzhi Tian, Harold Flanagan, Guanghui Wang

Abstract—This paper focuses on the mapping and rate of spread (ROS) measurement of grass fires using near infrared (NIR) images acquired by a small fixed-wing UAS operating at low altitudes. A new method is proposed for spatiotemporal representation of grass fire evolution using time labeled UAS NIR orthomosaics stitched from aerial images collected at varying time stamps over different regions of fire. Furthermore, a novel NIR intensity variance thresholding (IVT) method is proposed for accurate identification and delineation of grass fire fronts based on the obtained NIR mosaics in Digital Numbers (DN). The proposed methods are demonstrated and validated using UAS NIR imagery acquired over a prescribed tallgrass fire in Kansas (around 13 ha.). Three NIR short time-series orthomosaics are generated at a time interval of about two minutes with a spatial registration accuracy of 1.45 m (RMSE). The mean ROS for head, flank, and back tallgrass fires are measured to be 0.28 m/s, 0.1 m/s, and 0.025 m/s.

Index Terms—Grass fire, wildland fire, Unmanned aircraft system (UAS), multispectral remote sensing, fire front detection, fire behavior.

I. INTRODUCTION

FIRE spread metrics such as fire front location and fire rate of spread (ROS) are critical to understanding fire behavior and to making predictions in their potential behavior changes. These metrics are required for the reconstruction of digital twins of a fire event, data-based fire spread prediction, and the understanding of the impact of atmosphere, terrain, and fuel on the fire behavior [1]. During prescribed and wildfire operations, the fire behaviors can be estimated by empirically-designed or physics-based fire models, such as the Rothermel [2], the CSIRO [3], and wildland urban interface fire dynamics simulator (WFDS) [4] models. Although these models have been widely used to predict the fire ROS in many fuel types [5]–[8], one of the biggest challenges in their operational use is the lack of ground truth data for evaluation and validation. Additionally, the accuracy and reliability of these models are highly dependent on the quality of weather,

S. Gowravaram (gnsaket@gmail.com), H. Chao, Z. Lin, P. Tian, and H. Flanagan are with the Aerospace Engineering Department, University of Kansas, Lawrence, KS 66045, USA.
S. Parsons is with the Kansas Biological Suvey Center for Ecological Research, University of Kansas, Lawrence, KS, 66047, USA
T. Zhao is with University of California, Merced, CA 95343, USA.
M. Xin is with University of Missouri, Columbia, MO 65211, USA.
X. Hu is with Georgia State University, Atlanta, GA 30302, USA.
G. Wang is with Toronto Metropolitan University, Toronto, Ontario, Canada.
Corresponding: Haiyang Chao, (E)chaohaiyang@ku.edu.
Manuscript received December, 2022.

fuel, and terrain information during a fire event, which can be difficult to obtain. These concerns can be minimized with the help of direct and accurate fire spread measurements during an active fire event. For example, accurate measurements of fire front location and fire ROS of a benchmark wildland fire can greatly improve the evaluation, validation, and fine-tuning of the existing fire spread models. However, such direct fire measurements can be challenging to acquire, given the complex and highly dynamic nature of fire spread in varying atmospheric and field conditions such as wind, relative humidity, temperature, fuel characteristics, and terrain features [9].

Many fire ROS measurements in the literature come from indoor observations through table-top and wind tunnel experiments [10], [11] or ground observations through towers or booms, which are limited to small scales and may not accurately depict the fire spread behavior across landscape scales. Remote sensing data can enable the accurate mapping of fire behaviors in larger spatial scales, making them better suited for wildland fire measurements. Although satellite remote sensing plays a vital role in fire monitoring, the coarser spatiotemporal resolutions of most satellite data make them more suited for large fires (lasting more than a day) and applications such as fire hot spot detection [12]–[14] and fire damage assessment [15]. Measurements of fire ROS and fire front location of prescribed fires or wildfires that only last few or several hours can be better facilitated by airborne remote sensing. In fact, it has been suggested that spatial and temporal resolutions of 10 m and 10 min are desired for accurate data-enabled operational wildfire spread modelling and forecasting [1]. These finer resolutions are generally achievable by airborne remote sensing. In fact, most existing remote sensing-based fire ROS measurements use imagery from manned aircraft [16]–[20]. The collected airborne imagery can be post-processed for detection and extraction of fire fronts and ROS measurement. However, deploying manned aircraft over fires can be challenging due to adverse flying conditions (smoke and heat), limited flight path flexibility (to avoid turbulence), and high operating costs.

In recent years, small Unmanned Aircraft Systems (UAS) equipped with multispectral cameras are increasingly used in fire missions for applications including post-burn vegetation mapping [21], fire ignition [22], and fire detection [23]. Its applications in fire ROS measurements are still limited [24]. Small UAS are light-weight, easy to handle, and cost-effective,

making them very handy for fire ROS measurements at low altitudes (< 122 m Class G airspace in the US). Thermal cameras can be installed on these UAS for fire measurement due to their ability to see through smoke and measure temperature [24]. However, thermal cameras are generally quite expensive and have lower image resolution as compared to RGB and near infrared (NIR) cameras [25], both of which have been widely used by the UAS multispectral remote sensing community [26], [27]. NIR images can be used for certain fire sensing missions since they are not affected much by smoke occlusion compared with RGB images [28], and can detect a lot more features than typical thermal images which generally have lower pixel resolutions (e.g. 640×512 pix. or lower). The main challenge for NIR-based fire mapping is that it cannot detect temperature changes directly and may create difficulties in fire front detection. Researchers have worked on NIR-based fire detection using ground images [28], [29] and airborne images [20]. For instance, NIR aerial images are first converted to Normalized Difference Vegetation Index (NDVI) and then used for fire line detection and extraction in [20]. However, such methods often require radiometric calibration of aerial NIR imagery, which may not be feasible to many UAS researchers, especially during low-altitude fire sensing missions.

The objective of this paper is to develop a low-cost grass fire mapping and ROS measurement system using NIR aerial images from a fixed-wing UAS. The methods in this paper are demonstrated and validated using low-cost NIR UAS data set over a prescribed grass fire that was conducted at the University of Kansas Anderson County Prairie Preserve (ACPP) near Welda, KS. The main contributions of this paper are as follows.

1) A new method for spatiotemporal representation of grass fire evolution is proposed by introducing time labeled UAS NIR orthomosaics generated from aerial images with limited footprints.
2) A UAS prescribed fire data set over a tallgrass field in Kansas, including short time-series NIR orthomosaics and local weather and terrain measurements (https://cusl.ku.edu/Flight_Log).
3) A novel NIR intensity variance thresholding method for grass fire front classification and extraction using aerial imagery in digital numbers (DN).
4) Comprehensive results, discussions, and lessons learned using low-cost NIR nadir-view imagery for grass fire mapping and fire ROS measurements.

The developed NIR-based grass fire sensing system, methods, and data can greatly benefit many other researchers such as:

1) UAS remote sensing researchers and operators who want to collect grass fire spread data but cannot afford expensive thermal cameras.
2) Researchers who are interested in using UAS for monitoring and mapping the evolution of other fast-evolving environmental processes such as chemical leaks, flooding, and extreme weather.

3) Wildland fire managers or fire fighters who would like to have accurate predictions of grass fire behavior.
4) Grass fire behavior researchers and fire spread modeling researchers who need representative grass fire data sets.

II. PRESCRIBED FIRE AND UAS DATA

This section describes the prescribed grass fire and the UAS data that are used for the demonstration and analysis of the proposed methods.

A. Prescribed Grass Fire

A prescribed grass fire was conducted from 11:38 AM to 12:25 PM (US Central Time) on October 8, 2019 by the Kansas Biological Survey (KBS) [30] near Welda, KS. The burn site is a relatively flat rectangular field ($530m \times 250m$) with uniform fuel vegetation cover dominated by C4 tallgrass and a mixture of herbaceous forbs and legumes (shown in Fig. 1). A ring fire pattern was conducted by two fire setting teams using drip torches. The fire ignition was initiated near the center of the north boundary and terminated near the center of the south boundary, with one team travelling clockwise and the other travelling counterclockwise. The ignition process was completed at around 12:17:32 PM after which the fire evolved naturally in the field. The boundary of the fire field is shown in Fig. 1. There were some inconsistencies in the fire ignition pattern with the teams having to spend more time to ignite the northeast and northwest corners. The weather conditions during the burn were measured in the field as $73°F$ temperature with 41% relative humidity and 6.26 m/s prevailing wind from the south. The wind measurement is from a Campbell Scientific CSAT3B wind anemometer installed at 1.9 m above the ground level close to the east boundary of the fire field.

B. KHawk UAS Data

A KHawk 55 fixed-wing UAS was deployed over the prescribed fire for multispectral image acquisition. The KHawk 55 UAS is a low-cost multispectral remote sensing platform developed by the Cooperative Unmanned Systems Lab (CUSL) at the University of Kansas. It is equipped with a Ublox M8P Here GPS and a Pixhawk Cube autopilot [31], which can support both manual and autonomous flight. Key specifications are provided in Table I.

TABLE I: KHawk 55 UAS specifications

Description	Value
Take-off Weight	2.5 kg
Wingspan	1.4 m
Cruise Speed	20 m/s
Maximum Endurance	30 min
Typical Altitude	120 m

The KHawk UAS was equipped with a low-cost PeauPro82 modified GoPro Hero 4 Black camera for NIR video acquisition. This camera was modified with an 850 nm IR pass filter making it sensitive to light in the NIR spectrum and was operated in a video mode at a frame rate of 29.97 Hz with pixel resolution of 1080×1920 pix respectively (see Table II).
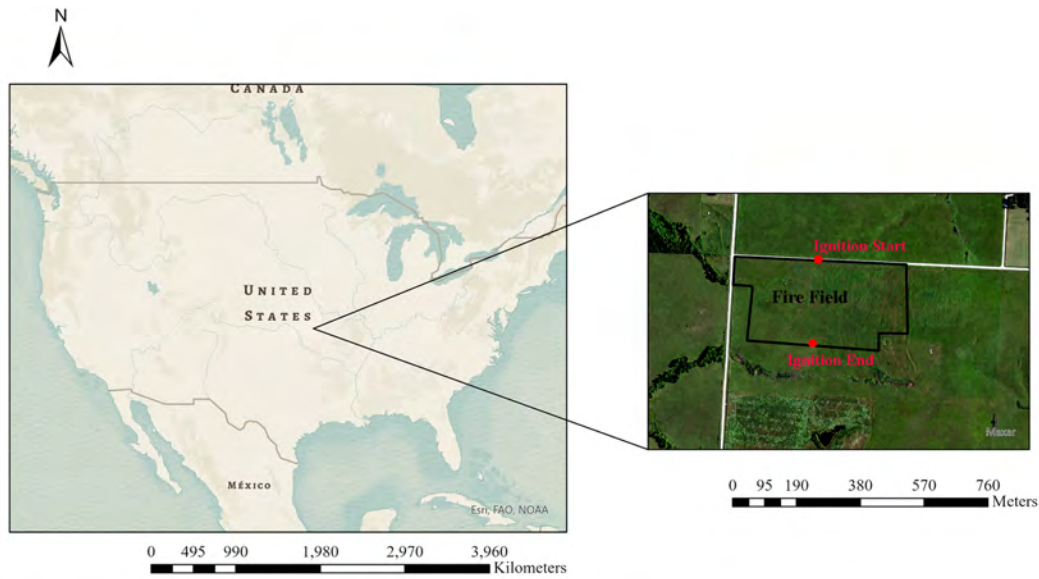
Fig. 1: Anderson County Prairie Preserve and the fire field.

Manual synchronization with the GPS logs is performed after the flight for image geotagging. Example images of the fire field are shown in Fig. 2.
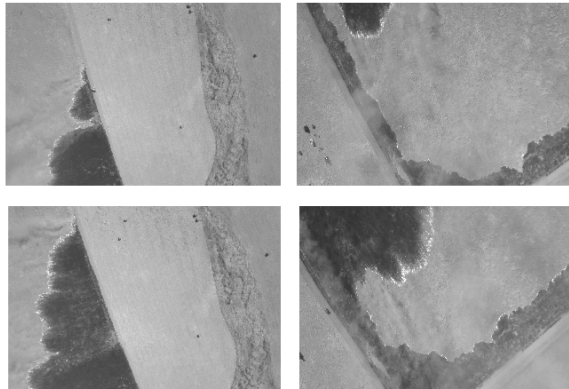

Fig. 2: PeauPro82 GoPro NIR images of fire field.

TABLE II: PeauPro82 Modified GoPro Hero 4 NIR Camera specifications.

Description	Value
Spectral Bandwidth	825.4 to 880 nm
Sensor Resolution	1920×1080 pix
Field-of-View (FOV)	$74° \times 45°$
Frame Rate	29.97 Hz
Spatial Resolution (at 120 m above the ground)	0.1 m

The KHawk UAS was programmed to fly multiple predetermined loops over the burning field at 120 m above the ground level to collect repeat-pass imagery of the burning field. It is worth mentioning that the UAS ground control station operator performed real-time adjustments to the predetermined flight path to follow the fire evolution based on ground fire observations. Repeat-pass imagery are defined as the images collected at the same location over the field at different time

steps. The objective of such a flight plan is to collect images for the generation of short time-series orthomosaics, where one orthomosaic corresponds to one flight loop. In this mission, the UAS completed one loop for 2 minutes and achieved 4 loops in total from about 12:06 PM to 12:18 PM. Three loops were used for orthomosaic generation to ensure map accuracy. The majority of the UAS flight path is overlaid on a National Agriculture Imagery Program (NAIP) image (spatial resolution of 1 m), shown in Fig. 3. The NAIP image was taken on June 30, 2019 and was used to geometrically register the UAS orthomosaics.
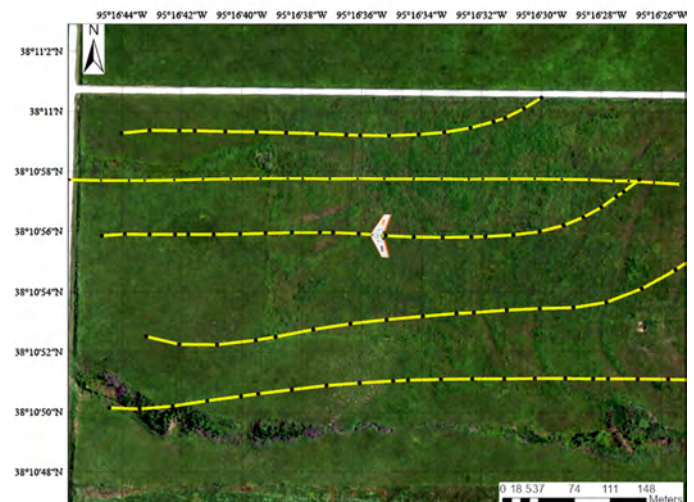

Fig. 3: KHawk 55 UAS flight path during the fire.

III. METHODS

This paper introduces a new method for the grass fire evolution mapping and ROS measurement using low-cost NIR images from a small UAS. The first part of this method focuses

on the spatiotemporal representation of the grass fire evolution using short time- series orthomosaics generated from repeat-pass images with limited footprints. In addition, time labeling is introduced for each grid within an orthomosaic to represent the different time stamps for UAS fire data acquisition. The second part is dedicated to fire front extraction from these orthomosaics using a novel NIR Intensity Variance Thresholding (IVT) method. Finally, these fire fronts are combined to form a fire evolution map that facilitates the calculation of the fire ROS.

A. Spatiotemporal Representation of the Fire Field Using Time-Labelled Orthomosaics

One of the main contributions of this paper is a new method for the spatiotemporal representation of the burning field using UAS short time-series orthomosaics with time labels. A small UAS flying at low altitudes generally observes only small patches of the burning field at a time, which is not ideal for the mapping and measurement of fire spread. For the spatial representation of the fire spread within a specific duration of time, images from each loop are grouped and orthorectified to form one orthomosaic. With the UAS collecting data in multiple loops over the fire field, short time-series orthomosaics can be generated [24] as shown in Fig. 4.
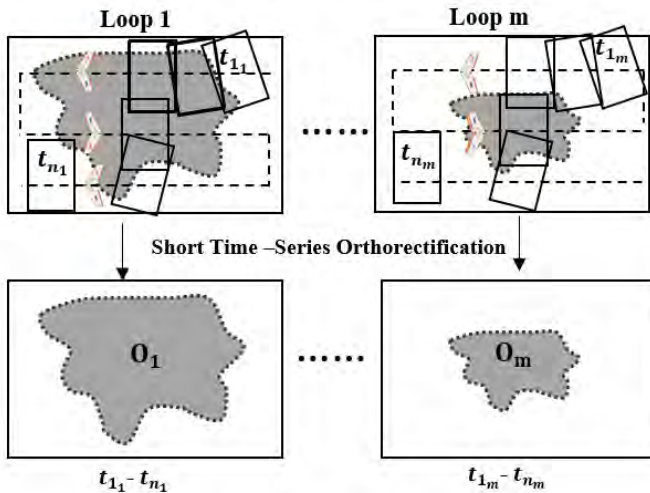
Fig. 4: Short time-series orthomosaic generation.

Since each orthomosaic is formed using multiple images collected at different times, a time interval can be assigned to each orthomosaic, where the starting and ending time corresponds to the time stamps of the first and last image in the loop, respectively. This is illustrated in Fig. 4. However, such time representation may not be enough for fire situational awareness and ROS calculation at finer scales. A new data representation is proposed in this paper to address this problem, with the basic idea shown in Fig. 5. Instead of using only one time step to represent the data acquisition time information for an orthomosaic, the orthomosaic will be divided into small zones with their own time labels. The size of each time zone and the time difference between them can be customized based on the desired temporal resolution,

camera footprint, overlapping percentage and ground speed of the UAS.

Given the UAS altitude of h above the ground and camera FOV of θ_x and θ_y, the size of one time zone in the orthomosaic can be computed as follows.

$$O_{m_t} = 2kh \tan \frac{\theta_x}{2} \times 2kh \tan \frac{\theta_y}{2}. \tag{1}$$

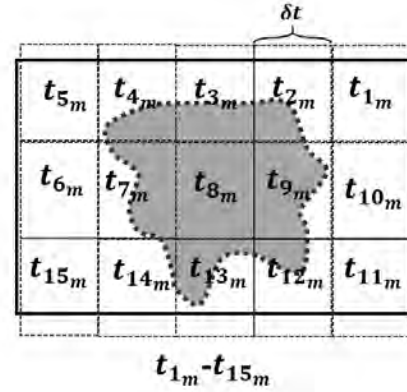where k is the scaling ratio between 0 and 1.

Fig. 5: Time labelling of fire field.

The generated orthomosaics can then be analyzed for fire front detection, extraction, and later fire evolution map generation.

B. NIR Intensity Variance Thresholding Method for Grass Fire Front Extraction

A new method is proposed for the fire front extraction problem based on airborne NIR imagery, which is called NIR Intensity Variance Thresholding (IVT) method. Given an NIR DN orthomosaic O_m with a size of $X \times Y$ pix., the IVT method can be used to identify and extract the pixels that represent the fire front, O_{m_f}. This method can be categorized into three steps, 1) image grid generation and fire grid classification, 2) fire front extraction, and 3) fire front manual delineation as illustrated in Fig. 6. The main advantage of this method comes from its use of NIR images in DN which does not require vicarious radiometric calibration efforts as the reflectance images.

1) Fire Grid Classification: The main objective of this step is to generate grids (see second row of Fig. 6) in an orthomosaic and classify them as fire and non-fire grids. O_m can be divided into n equally spaced grids of dimensions $x \times y$ pix. The size of the grid can be determined based on the following two criteria.

- Maximum flame depth for grass fire. Flame depth is defined as the distance from the leading edge to the trailing edge of the flaming front [32]), which can be estimated from UAS NIR orthomosaics. One of the fundamental requirements of our IVT algorithm for successful fire grid classification is that the grids encapsulate pixels corresponding to unburned, burned, and fire regions. This is because the IVT algorithm relies on the intensity
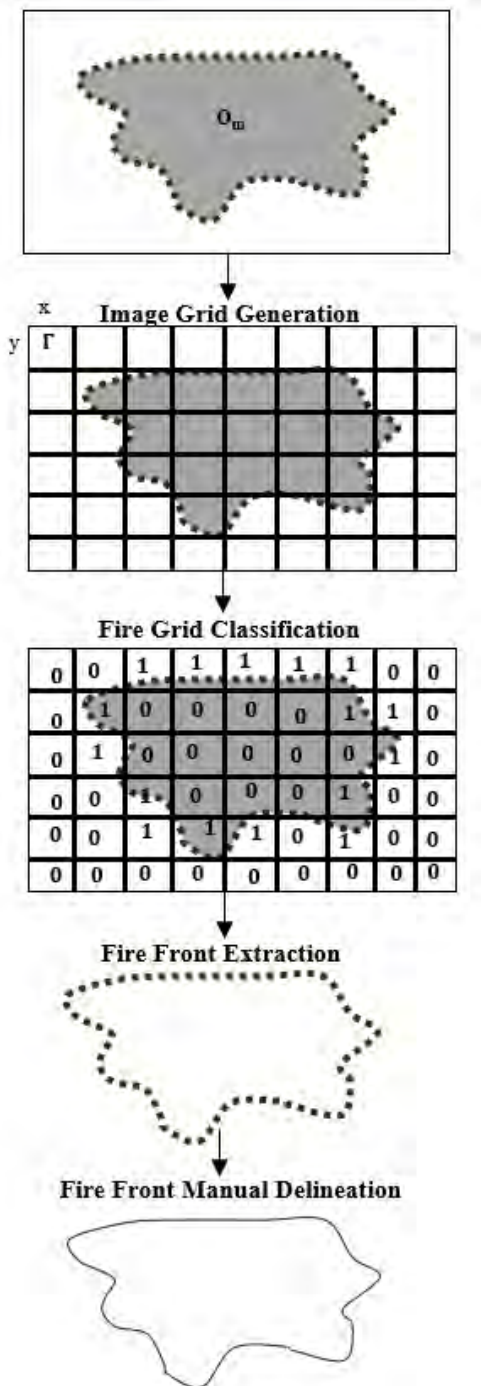
Fig. 6: Intensity variance thresholding method.

distribution pattern within a grid to differentiate between non-fire and fire grids. Therefore, the size of the grid has to be larger than the maximum flame depth as observed in NIR orthomosaics. We recommend that the grid size be at least 2 times of the maximum flame depth. For example, if the observed maximum flame depth is 4 m, a minimal grid size of 8 m is suggested.

- Minimizing outliers for fire front detection. One of the main challenges for using NIR DN orthomosaics for fire extraction is the presence of outliers or noisy pixels.

Uncalibrated NIR orthomosaics tend to have random pixels that have very high intensity values. This can lead to the IVT algorithm falsely classifying these outlier pixels as fire, since NIR fire pixels also saturate or hold at very high intensity values. There will be more outlier pixels when the grid size increases. Multiple trials can be performed at different grid sizes starting from the minimal value provided in the above criteria 1. A final value can be selected for a balance of accuracy, computational cost, and spatial resolution.
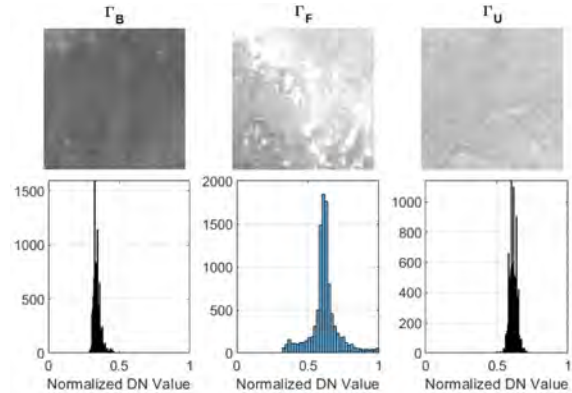

Fig. 7: Examples of burned (left), fire (center), and unburned (right) grids and their respective histograms (bottom).

After selection of the grid size, the next step is to generate grids and perform pixel classification. The main difference between the non-fire grids (Γ_U and Γ_B) and fire grids (Γ_F) is that, Γ_F contain pixels of unburned grass, burned grass, and the fire, while Γ_U and Γ_B only contain either unburned or burned grass pixels. Given that fire is represented as very high values or even saturated values in NIR images, the fire grids are expected to demonstrate a higher variability in pixel distribution, as compared to non-fire grids. Additionally, the fire grids also demonstrate a higher pixel range (difference between maximum and minimum pixel intensity within a grid). This can be observed in Fig. 7, where Γ_F shows a wider range and a higher variability as opposed to Γ_U and Γ_B. Note that this figure shows the grids in normalized (0-1) DN values.

An orthomosaic, O_m can be classified into non-fire grids and fire grids Γ_F based on the distribution of all pixels enclosed within each grid. Two thresholds, α and β can be defined pertaining to the coefficient of variation CV and range R of each grid as the classification criteria. Here, CV_Γ is defined as the ratio of standard deviation σ_Γ and mean μ_Γ and R_Γ is defined as the difference between the maximum and minimum pixel values within a grid Γ. The grids that satisfy the α and β criteria are classified as fire grids, Γ_F with a value of 1, while all other grids are classified as non-fire grids with a value of 0.

$$\Gamma = \begin{cases} 1, & \text{if } CV_\Gamma \geq \alpha \ \& \ R_\Gamma \geq \beta, \\ 0, & \text{otherwise.} \end{cases} \qquad (2)$$
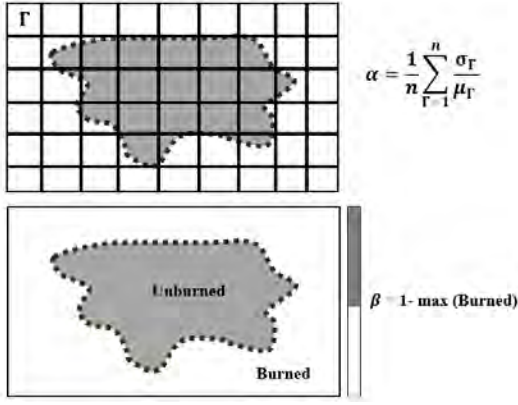
Fig. 8: Fire grid classification thresholds: α (L) and β (R).

α-*Selection:* The α threshold is to classify grids based on the extent of pixel intensity variability within the grid using the coefficient of variation CV. The α can be selected as the mean CV of all the grids.

$$\alpha = \frac{1}{n}\Sigma_{\Gamma=1}^{n}CV_{\Gamma} \tag{3}$$

β-*Selection:* The β threshold is to classify grids based on the range of pixel intensity values within the grid. The β is determined empirically using the distribution of pixels in the orthomosaic O_m. The maximum pixel intensity value in O_b corresponding to the burned areas is used to calculate β.

$$\beta = 1 - max(O_{m,B}) \tag{4}$$

where, $O_{m,B}$ denotes the pixel intensity values in O_m that represent the burned areas (low-intensity).

The reason for using the pixel intensity variation and range criteria is to ensure that the algorithm observes the distribution of all the pixels within a grid and not just the minimum and maximum values. For example, if only the range criterion is used, grids with smoke occlusion or saturated pixels may wrongly be classified as fire grids. It is also worth mentioning that this algorithm observes the differences in distribution characteristics between fire and non-fire grids and does not depend on the absolute histogram distribution of the pixel intensity values. This algorithm is expected to successfully differentiate between fire and non-fire grids even if the pixel intensity values of grass are lower or higher, which can happen during different growing stages of the grass.

2) Fire Front Extraction: Given the identified fire grids in $x \times y$ pix. region, the next step is to locate the fire pixels within these regions for fire front extraction. This is also achieved using the pixel distribution within the fire grids. Since these grids exhibit a Gaussian distribution (shown in Fig. 7) and the maximum pixel values enclosed within them can be identified as fire pixels, a threshold γ can be defined based on the empirical rule of a Gaussian distribution. The pixels within each Γ_F that satisfy the γ rule is classified as fire pixels.

$$O_{m_f} = \begin{cases} 1, & \text{if } \Gamma_{F_{x,y}} \geq (\mu_{\Gamma_F} + \gamma\sigma_{\Gamma_F}) \\ 0, & \text{otherwise,} \end{cases} \tag{5}$$

where, $\Gamma_{F_{x,y}}$ is a pixel value at a geolocation (x,y) within a grid Γ_F and γ is an empirically selected value.

The value of γ is empirically selected between 2 and 3, these values correspond to values above 95 % for the Gaussian distribution (68-95-99.7 rule).

3) Fire Front Manual Delineation: As illustrated in Fig. 6, the fire front extraction algorithm can isolate fire pixels that are often discrete and undesirable for later fire evolution mapping and ROS measurement. The extracted fire front pixels can be manually joined to form a continuous fire front curve for better representation.

C. Fire Evolution Mapping

The delineated fire fronts from each orthomosaic are then combined to form a fire evolution map. The main components of this map include, the fire front locations, associated time labels, and their spread direction vectors. For the spread direction vectors, a normal to the curve approach is used which is generally defined as the direction of the spread of a fire front [20], [33], [34]. An example of such a map is shown in Fig. 9.
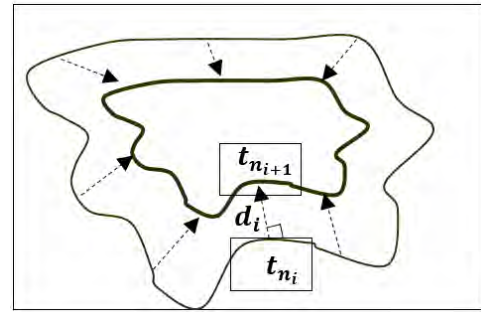

Fig. 9: Fire evolution map and ROS calculation.

The fire evolution map contains the information required to calculate the ROS for any given point along a fire front, including the spread distance, d_i and the time difference, $(t_{n_{i+1}} - t_{n_i})$ as shown in Fig. 9.

IV. RESULTS

The methods described in Sec. III are demonstrated using a GoPro NIR video collected by the KHawk 55 fixed-wing UAS over a Kansas prescribed grass fire. Detailed results and analyses are presented in this section.

A. Spatiotemporal Representation of the Fire Field Using Time-Labelled Orthomosaics

Repeat-pass individual frames are extracted from the NIR video and grouped accordingly for the generation of short time-series orthomosaics as shown in Fig. 10. Each orthomosaic is generated from about 120-150 images using the same processing parameters in the Agisoft Photoscan Pro software. Using the time labelling descriptions and formulations provided in Sec. III.A, each orthomosaic was roughly divided into 190 m × 110 m areas with a difference around 5 seconds.

Fig. 10: NIR short time-series orthomosaics.

TABLE III: Short Time-Series NIR Orthomosaic Properties.

Orthomosaic	Number of Images	Time Interval (Central)
O_1	147	$12:07:03 - 12:09:19$ PM
O_2	133	$12:12:41 - 12:15:03$ PM
O_3	119	$12:15:26 - 12:17:47$ PM

Table III shows the number of images used and corresponding time intervals for each orthomosaic.

The orthomosaics shown in Fig. 10 are registered with a NAIP image with a spatial resolution of 1 m using the ArcGIS Georeferencing tool. Note that the NAIP image was acquired on June 30, 2019 and has a 95 % confidence accuracy of around 6 m [35]. Control point pairs between each orthomosaic and the NAIP image were manually selected such that they covered the whole field. All the orthomosaics were registered using an Affine transformation and achieved a root mean square error (RMSE) of about 1.3 to 1.45 m, as shown in Table IV.

TABLE IV: Image-to-Image Registration Attributes for Short Time-Series NIR Orthomosaics Using 1 m NAIP Imagery.

Orthomosaic	Spatial Resolution (m)	Control Point Pairs	RMSE (m)
O_1	0.1	9	1.45
O_2	0.1	9	1.3
O_3	0.1	10	1.37

B. NIR-based IVT Method for Fire Front Extraction

The proposed IVT method (Sec. III.B) is then implemented on the registered NIR orthomosaics for fire front extraction. First, initial analyses are performed to determine a reasonable grid size. We observed that our algorithm generated similar results for the grid size between 10 and 20 m. A grid size of 10×10 m (or 100×100 pix.) is selected considering multiple factors such as accuracy and computational efficiency. The registered orthomosaics are divided into equally spaced grids Γ. Then, the pixel distribution within each grid Γ is analyzed for fire grid classification. The NIR orthomosaics are normalized to 0-1 range, shown in Fig. 10. The α and β are selected as 0.02 and 0.6 respectively. All the grids with CV greater than 0.02 and range greater than 0.6 are classified

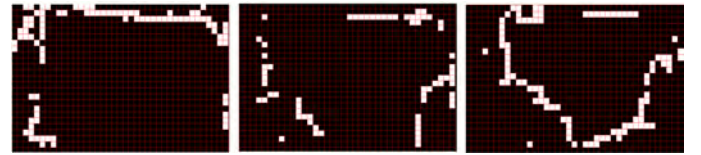as fire grids, while all the other grids are classified as non-fire grids, as shown in Fig. 11.

Fig. 11: Fire grid classification.

The fire grids are then searched for fire pixels using (4), where all pixels within a grid that satisfy the γ condition are classified as fire pixels while all other pixels are classified as non-fire pixels. It was found that the fire pixels within the classified fire grids represented the 95th percentile and above values. Therefore, γ was selected to be 2. Fig. 11 shows the extracted fire fronts from each orthomosaic. Finally, these fire front pixels are manually delineated using a line feature class in ArcGIS pro to form continuous fire front curves.

C. Validation of Fire Front Extraction

Qualitative and quantitative validation analyses were conducted to show the effectiveness of the proposed IVT method. For qualitative validation, popular edge detection methods including, the Canny and LoG methods [36] are applied to the NIR orthomosaics and the results are visually compared to those generated by the proposed method. The objective of this analysis is to illustrate the effectiveness of the proposed method in rejecting noisy pixels such as saturated and smoke pixels that are not often rejected by existing edge detection methods. The Canny, LoG edge detection, and the proposed IVT methods are applied to O_2 and shown in Fig. 13. From this figure, it is evident that proposed IVT method performs better than the existing edge detection methods for fire front extraction from high-resolution (0.1 m) NIR DN images. The main reason is that the IVT first identifies fire regions at a coarser resolution and then applies the fire front extraction algorithm to only those areas which rejects outliers that are often a problem when searching for the fire front directly in high-resolution images.

For quantitative validation, the IVT extracted fire fronts are compared to manually extracted fire fronts from the
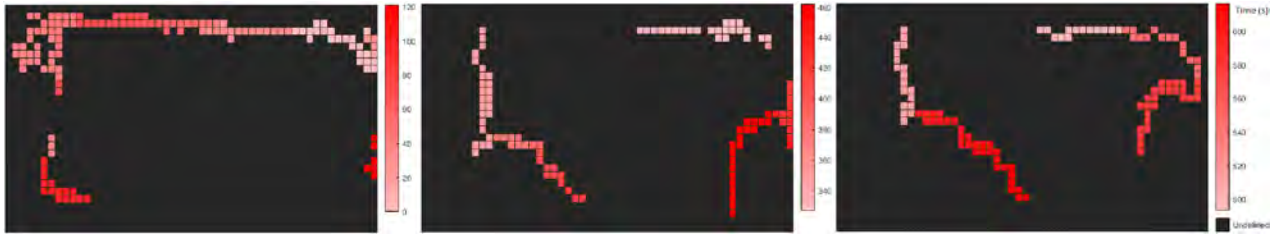
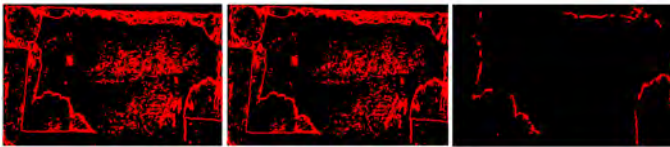Fig. 12: Time labeled orthomosaics (12:07:03-12:17:47 PM).

Fig. 13: Qualitative comparison between fire fronts from Canny(left), LoG edge detection(center), and IVT methods (right).

orthomosaics. The minimum distance between the manual and IVT fire fronts are compared for error quantification. This analysis is conducted on all the NIR orthomosaics and the resulting errors are tabulated in Table V. It can be observed that the mean errors for each orthomosaic are less than or around 1 m. This error is reasonable and does indicate that the IVT is effective in accurately extracting the fire fronts.

TABLE V: Fire Front Error Statistics.

Orthomosaic	Min	Mean	Max	Std.
O_1	0.01	0.46	1.61	0.35
O_2	0.002	1.01	7.52	1.05
O_3	0.002	1.01	3.52	1.05

D. Fire Evolution Mapping

The extracted and delineated fire front curves, f_1, f_2, f_3 are then combined to form a fire evolution map which provides information about the fire front location, spread direction, and the ROS. Fig. 14 shows the fire evolution map with labels defining the head fire, flank fire, and back fire. Certain regions with stitching inconsistencies are excluded from the fire ROS analysis such as the west and east fire fronts of f_1, which are the overlapping areas of the two flight lines.

The fire fronts shown in Fig. 14 are categorized into head, flank, and back fires based on the spread directions. Since the prevailing wind during the fire is from the south at about 6.26 m/s (measured at around 2 m above the ground level), the fire fronts spreading north are categorized as the head fire, while the fire fronts spreading east or west are categorized as the flank fire, and the fire fronts spreading south are categorized as back fire.

The fire fronts with defined spread vectors are used to calculate the ROS. For analysis, the head and flank fire fronts

are divided into two categorizes based on spread direction, NE, NW for the head fire front and E, W for the flank fire front. Note that these categories indicate the direction towards which the fire front is spreading. For example, the portion of head fire front spreading towards the NE is categorized as a NE fire front. The back fire ROS is calculated between f_1 and f_3. The ROS between these fire fronts are calculated as described in Sec. III.C and tabulated in Tables VI, Table VII, and , Table VIII.

TABLE VI: Head Fire ROS Statistics.

Fire Fronts	Min	Mean	Max	Std.
$f_1 - f_{2\,NE}$	0.21	0.24	0.25	0.016
$f_2 - f_{3\,NE}$	0.18	0.26	0.35	0.05
$f_2 - f_{3\,NW}$	0.27	0.45	0.44	0.07
Cumulative				
	0.18	0.28	0.44	0.07

TABLE VII: Flank Fire ROS Statistics.

Fire Fronts	Min	Mean	Max	Std.
$f_1 - f_{2\,E}$	0.04	0.06	0.07	0.001
$f_2 - f_{3\,E}$	0.03	0.06	0.09	0.02
$f_2 - f_{3\,W}$	0.02	0.1	0.2	0.06
Cumulative				
	0.02	0.1	0.2	0.06

TABLE VIII: Back Fire ROS Statistics.

Fire Fronts	Min	Mean	Max	Std.
$f_1 - f_3$	0.0136	0.025	0.0435	0.0106

From these tables, it can be observed the mean head fire, flank fire, and back fire ROS are measured to be 0.28 m/s, 0.1 m/s, and 0.025 m/s respectively. The measured ROS are further visualized in a polar plot, as shown in Fig. 15.

V. DISCUSSIONS & LESSONS LEARNED

Critical insights, in-depth discussions, and lessons learned from the proposed method and implementations are provided in this section.

A. Accuracy in Time labelling and Spatiotemporal Representation

There exist several challenges in evaluating and analyzing the accuracy of the proposed spatiotemporal representation including handling of multiple overlapping aerial images looking
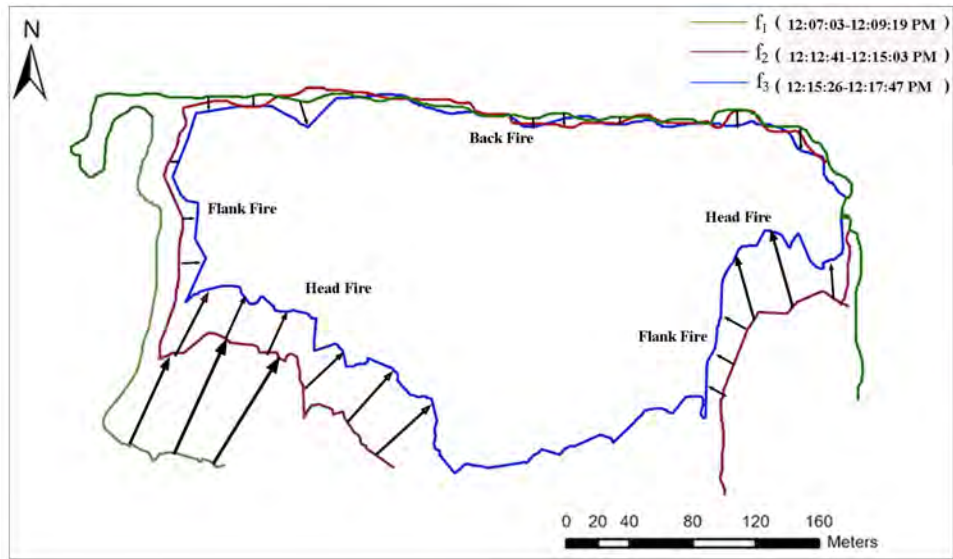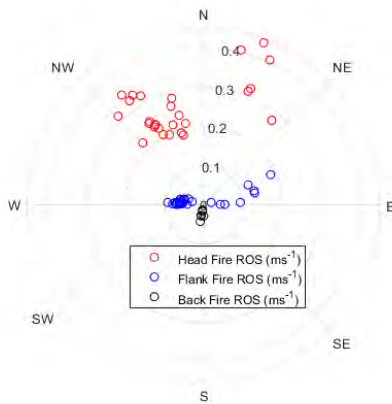
Fig. 14: Fire evolution map.

Fig. 15: ROS polar plot.

at the same grid and accurate labeling of fire front location. For our UAS fire data set, the fire front in one grid may show up in about 7 overlapping images on average ($\sim$ 0.7 sec. time difference between two consecutive images), which raised the challenges in time and spatial accuracy analysis within each fire front grid. The 0.7 sec. difference is mostly determined by the longitudinal overlapping percentage of the orthomap, the camera fps, and the UAS ground speed. For our data set, the time difference in 7 overlapped images may result in about ±2.5 sec. uncertainty in time. Since our UAS flies much faster ($\sim$ 25 m/s) than the fire spread (0.01-0.4 m/s), we can assume that the movement of the fire is trivial within the overlapped pictures. Second, manual corrections of fire labeling are sometimes needed since fire lines identified by IVT method may generate minor errors especially when the fire front is at the boundary of the grid. However, the correction may only shift fire front one grid away from the identified fire front. Finally, the acquired time stamp information using the proposed spatiotemporal representation is compared with the ones derived using the manual approach based on the thermal image dataset from the same prescribed fire [24]. The average time difference between spatiotemporal representation and the manual approach is 0.88 sec., which falls in the ±2.5 sec. uncertainty bound.

B. Fire ROS Accuracy

The accuracy of the fire ROS measurements is critical to wildfire management, prescribed fire planning and policy making, and fire behavior model validation. Our fire ROS accuracy is analyzed from three sides, uncertainty analysis, literature data, and cross validation with thermal data. The uncertainty of our fire ROS measurements comes from both the fire front location and the elapsed time between the two fire front lines. The spatial position accuracy of the NIR fire front location is about 1.45 m (RMS, $1-\sigma$). Assume that the elapsed time between two fire lines is around 120 seconds, the fire ROS uncertainty will be around 0.024 m/s. This means that our head fire and flank fire ROS estimates are fairly accurate while the back fire ROS needs further confirmation. In addition, our measured grass fire ROS matches with the expected grass fire behavior in Kansas based on NWS researchers' former work where a fire ROS of 0.18/0.36 m/s corresponds to a grass fire danger index of 5/10 with moderate/high difficulty of suppression [37]. Considering the strong prevailing wind velocity that day ($\tilde{6}$ m/s), it is not surprising that the fire danger is relatively high. Finally, the NIR derived fire ROS estimates agree with the thermal derived fire ROS from the same prescribed fire [24]. In fact, thermal cameras are more widely used for wildland fire ROS measurement in the literature [16], [34], [38]. The mean head fire and flank fire ROS for thermal data are measured to be 0.27 and 0.11 m/s [24], which have a 0.01 m/s difference for both data and are within the 0.024 m/s uncertainty bound.

C. Using UAS Orthomosaic to Monitor a Slowly Evolving Process

UAS orthomosaics have been widely used for mapping of static scenes. Our dataset and method showed that they can be extended to monitoring and mapping of slowly evolving processes such as a grass fire (compared with the fast UAS flying speed). The following are observed and suggested based on our experience.

a) Feature matching and stitching: Feature matching among the longitudinal and lateral overlapped images are key to the generation of accurate orthomosaics. Since our UAS generally flies at a much faster ground speed (20-30 m/s) than the grass fire evolution (0.025-0.28 m/s mean ROS), the scene only changes slightly among the aerial images used for stitching. The feature matching among these aerial images is sufficient for the stitching process, which is shown by the small stitching error (< 1.5 m RMSE). For our grass fire data set, the biggest error comes from the lateral overlapping areas when there is a fireline. This can be observed from the middle left of the fire front in the left subfigure of Fig. 10, which generated blurred fire front. Nevertheless, the stitching can still be achieved since the affected regions only cover a small portion of the overlapped areas. These blurred fire fronts are not used in the fire metrics analysis.

b) Time labelling: One of the novelties of this paper is the introduction of the time labelling compared with the conventional orthomosaics. The time labels for different fire grids within an orthomosaic can potentially be used for data-based fireline prediction and correction so that an improved UAS orthomap can be generated with the same timestamp across all the fire lines. This will be one future direction of our work.

D. Other Factors Affecting the Accuracy of UAS-based Fire Metrics Measurements

The accuracy of UAS derived fire maps (for example, Fig. 14) is affected greatly by the quality of the aerial images and corresponding GPS location data collected by the UAS when flying over the evolving fire. The quality of these data may be affected by many UAS flight performance metrics such as orientation tracking errors, flight speed, UAS flight trajectory, and the specification and setting of sensing payloads (cameras and GPS). Two key factors, the UAS flight trajectory and the sensor accuracy are discussed in details below.

a) UAS flight trajectory: Fire missions designed for accurate fire mapping and fire ROS measurement require high-quality observations of the fire front at regular time intervals, which can be used to generate consistent time-series orthomosaics. For prescribed fire experiments (similar to the Anderson county grass fire shown in this paper), an ideal UAS flight trajectory is to fly wings-level and steady in consistent loops over the fire field at regular time intervals while capturing images of the burning field. For example, a UAS needs to fly over the same front at time t_0, $t_1 = t_0 + \delta t$, and so on, where δt is the time taken by the UAS to complete one loop. This way, the UAS can capture the evolution of fire fronts in the region at regular time intervals which can

be used for fire metrics measurements such as fire ROS. However, such a flight trajectory can be difficult to achieve due to multiple reasons such as irregular fire evolution patterns and fire-induced turbulence, such as thermals. Fire-generated weather can also affect the orientation of the UAS, which can consequently result in the capturing of oblique and blurry images that may not be usable in the orthomosaic stitching. An example of such a scenario can be seen in the rightmost image in Fig. 10. The gap near the top right portion of this image was caused by rejecting blurry images (due to oscillating UAS roll angles during capture) from the stitching process.

b) Sensor properties: The properties of operating sensing payload, such as cameras and GPS play a vital role in the accuracy of UAS data derived fire metrics. Camera properties include frames per second (fps), image resolution, and FOV. Higher fps can achieve more frequent observations of the fire, while higher image resolution and FOV can achieve better spatial representations of the burning field. It is worth emphasizing that spectral properties of the images also play a crucial role in dictating the accuracy of the delineated fire front locations. For example, fire fronts within thermal images are easier to delineate than those in NIR images, while NIR images are less susceptible to smoke occlusion than RGB images and are sensitive to the charring of vegetation in the burning field. The IVT method proposed in this paper extracts the fire front from NIR images using this property. It is worth mentioning that these camera properties only control the accuracy of fire front locations in the image coordinate frame. The locations and the ROS of the extracted fire fronts in the world coordinate frame (latitude and longitude) are directly affected by the accuracy of the GPS data onboard the UAS. This can be overcome by using cm-level RTK GPS or by performing image-to-image registration using reference images. In this paper, the resulting fire maps are accurate up to 1.5 m since the time-series orthomosaics were registered using a 1-m NAIP reference image.

VI. Conclusions & Future Work

This paper describes a novel NIR-based grass fire mapping and ROS measurement method that uses UAS short time-series orthomosaics with time labels. This method uses low-cost NIR cameras instead of expensive thermal cameras, which are feasible to many UAS operators. Moreover, the proposed method is developed for DN images and does not require vicarious radiometric calibrations that can be challenging for UAS images. This method was demonstrated using a GoPro NIR video that was collected by KHawk fixed-wing UAS when flying multiple loops over a prescribed grass fire (530 m $\times$ 250 m) in Welda, KS and yielded an accurate fire evolution map (about 1.5 m registration error compared to the NAIP image), using three NIR short time-series orthomosaics at regular time intervals (about 2 minutes). Finally, we determined that this prescribed grass fire had mean head fire, flank fire , and back fire ROS of 0.28 m/s, 0.1 m/s, and 0.025 m/s respectively.

Future goals for fixed-wing UAS based fire evolution mapping and ROS measurement include, 1) fully automatic fire front detection using supervised learning, 2) real-time

fire mapping and ROS measurement for better fire situation awareness, 3) autonomous UAS path adjustments based on onboard fire spread measurements, and 4) integration of cm-level RTK GPS on-board the UAS and use of GCP for improved orthorectification, 5) generation of the guidelines for using UAS orthomosaics to monitor a slowly evolving process through comprehensive analysis and studies.

REFERENCES

[1] M. Gollner, A. Trouve, I. Altintas, J. Block, R. de Callafon, C. Clements, A. Cortes, E. Ellicott, J. B. Filippi, and M. Finney, "Towards data-driven operational wildfire spread modeling: a report of the NSF-funded WIFIRE workshop," Tech. Rep., 2015.

[2] R. C. Rothermel, *A Mathematical Model for Predicting Fire Spread in Wildland Fuels.* Intermountain Forest & Range Experiment Station, Forest Service, US, 1972, vol. 115.

[3] M. Cruz, J. Gould, M. Alexander, A. Sullivan, W. McCaw, and S. Matthews, "A guide to rate of fire spread models for Australian vegetation. revised edition," 2015.

[4] W. E. Mell, R. J. McDermott, and G. P. Forney, "Wildland fire behavior modeling: perspectives, new approaches and applications," in *Proceedings of 3rd fire behavior and fuels conference, Spokane, Washington, USA*, 2010, pp. 45–62.

[5] J. H. Scott, *Standard Fire Behavior Fuel Models: A Comprehensive Set for Use with Rothermel's Surface Fire Spread Model.* US Department of Agriculture, Forest Service, Rocky Mountain Research Station, 2005.

[6] N. Cheney, J. Gould, and W. R. Catchpole, "Prediction of fire spread in grasslands," *International Journal of Wildland Fire*, vol. 8, pp. 1–13, 1998.

[7] I. Noble, A. Gill, and G. Bary, "Mcarthur's fire-danger meters expressed as equations," *Australian Journal of Ecology*, vol. 5, no. 2, pp. 201–203, 1980.

[8] N. Cheney, J. Gould, and W. Catchpole, "The influence of fuel, weather and fire shape variables on fire-spread in grasslands," *International Journal of Wildland Fire*, vol. 3, no. 1, pp. 31–44, 1993.

[9] NWCG. (2022) National Wildfire Coordinating Group. [Online]. Available: https://www.nwcg.gov/

[10] M. Finney, J. Cohen, I. Grenfell, and K. Yedinak, "An examination of fire spread thresholds in discontinuous fuel beds," *International Journal of Wildland Fire*, vol. 19, no. 2, pp. 163–170, 2010.

[11] E. Marino, J. Dupuy, F. Pimont, M. Guijarro, C. Hernando, and R. Linn, "Fuel bulk density and fuel moisture content effects on fire rate of spread: A comparison between FIRETEC model predictions and experimental results in shrub fuels," *Journal of Fire Sciences*, vol. 30, no. 4, pp. 277–299, 2012.

[12] W. Schroeder, E. Prins, L. Giglio, I. Csiszar, C. Schmidt, J. Morisette, and D. Morton, "Validation of GOES and MODIS active fire detection products using ASTER and ETM+ data," *Remote Sensing of Environment*, vol. 112, no. 5, pp. 2711–2726, 2008.

[13] I. A. Csiszar, J. T. Morisette, and L. Giglio, "Validation of active fire detection from moderate-resolution satellite sensors: the MODIS example in northern Eurasia," *IEEE Transactions on Geoscience and Remote Sensing*, vol. 44, no. 7, pp. 1757–1764, 2006.

[14] I. Csiszar, W. Schroeder, L. Giglio, E. Ellicott, K. P. Vadrevu, C. O. Justice, and B. Wind, "Active fires from the Suomi NPP visible infrared imaging radiometer suite: product status and first evaluation results," *Journal of Geophysical Research: Atmospheres*, vol. 119, no. 2, pp. 803–816, 2014.

[15] K. Badarinath, A. Sharma, and S. Kharol, "Forest fire monitoring and burnt area mapping using satellite data: A study over the forest region of Kerala State, India," *International Journal of Remote Sensing*, vol. 32, no. 1, pp. 85–102, 2011.

[16] D. Stow, P. Riggan, E. Storey, and L. Coulter, "Measuring fire spread rates from repeat pass airborne thermal infrared imagery," *Remote Sensing Letters*, vol. 5, no. 9, pp. 803–812, 2014.

[17] R. S. Allison, J. M. Johnston, G. Craig, and S. Jennings, "Airborne optical and thermal remote sensing for wildfire detection and monitoring," *Sensors*, vol. 16, no. 8, p. 1310, 2016.

[18] P. Riggan, R. Tissell, R. Lockwood, J. Brass, J. Pereira, H. Miranda, A. Miranda, T. Campos, and R. Higgins, "Remote measurement of energy and carbon flux from wildfires in Brazil," *Ecological Applications*, vol. 14, no. 3, pp. 855–872, 2004.

[19] O. Viedma, F. Chico, J. Fernández, C. Madrigal, H. Safford, and J. M. Moreno, "Disentangling the role of prefire vegetation vs. burning conditions on fire severity in a large forest fire in SE Spain," *Remote Sensing of Environment*, vol. 247, p. 111891, 2020.

[20] A. E. Ononye, A. Vodacek, and E. Saber, "Automated extraction of fire line parameters from multispectral infrared images," *Remote Sensing of Environment*, vol. 108, pp. 179–188, 2007.

[21] P. McKenna, P. D. Erskine, A. M. Lechner, and S. Phinn, "Measuring fire severity using UAV imagery in semi-arid central Queensland, Australia," *International Journal of Remote Sensing*, vol. 38, no. 14, pp. 4244–4264, 2017.

[22] E. Beachly, C. Detweiler, S. Elbaum, D. Twidwell, and B. Duncan, "UAS-Rx interface for mission planning, fire tracking, fire ignition, and real-time updating," in *2017 IEEE International Symposium on Safety, Security and Rescue Robotics (SSRR)*. IEEE, 2017, pp. 67–74.

[23] S. Gowravaram, H. Chao, H. Flanagan, P. Tian, J. Goyer, M. Xin, and X. Hu, "Wildland fire monitoring and mapping using orthorectified near-infrared and thermal UAS imagery," in *101st American Meteorological Society Annual Meeting*. AMS, 2021.

[24] S. Gowravaram, H. Chao, T. Zhao, S. Parsons, X. Hu, M. Xin, H. Flanagan, and P. Tian, "Prescribed grass fire evolution mapping and rate of spread measurement using orthorectified thermal imagery from a fixed-wing UAS," *International Journal of Remote Sensing*, vol. 43, no. 7, pp. 2357–2376, 2022.

[25] S. Khanal, J. Fulton, and S. Shearer, "An overview of current and potential applications of thermal remote sensing in precision agriculture," *Computers and Electronics in Agriculture*, vol. 139, pp. 22–32, 2017.

[26] S. Gowravaram, H. Chao, A. Molthan, T. Zhao, P. Tian, H. Flanagan, L. Schultz, and J. Bell, "Spectral reflectance estimation of uas multispectral imagery using satellite cross-calibration method," *Photogrammetric Engineering & Remote Sensing*, vol. 87, no. 10, pp. 735–746, 2021.

[27] S. Gowravaram, P. Tian, H. Flanagan, J. Goyer, and H. Chao, "Uas-based multispectral remote sensing and ndvi calculation for post disaster assessment," in *2018 International Conference on Unmanned Aircraft Systems (ICUAS)*. IEEE, 2018, pp. 684–691.

[28] J. D. Burnett and M. G. Wing, "A low-cost near-infrared digital camera for fire detection and monitoring," *International Journal of Remote Sensing*, vol. 39, no. 3, pp. 741–753, 2018.

[29] M. A. Akhloufi, T. Toulouse, and L. Rossi, "Multiple spectrum vision for wildland fires," in *Thermosense: Thermal Infrared Applications XL*, vol. 10661. International Society for Optics and Photonics, 2018, p. 1066105.

[30] KBS. (2022) Kansas Biological Survey. [Online]. Available: https://biosurvey.ku.edu/field-station

[31] ArduPilot2021. (2021) Pixhawk. [Online]. Available: https://ardupilot.org/

[32] U. S. F. S. (USFS), "Flame descriptors," 2021, digital media. [Available online at https://southernfireexchange.org/wp-content/uploads/2013-6.pdf.].

[33] S. Pyne, P. Andrews, and R. Laven, *Introduction to Wildland Fire.* John Wiley and Sons, 1996.

[34] D. Stow, P. Riggan, G. Schag, W. Brewer, R. Tissell, J. Coen, and E. Storey, "Assessing uncertainty and demonstrating potential for estimating fire rate of spread at landscape scales based on time sequential airborne thermal infrared imaging," *International Journal of Remote Sensing*, vol. 40, no. 13, pp. 4876–4897, 2019.

[35] USDA, "National agriculture imagery program," 2009, digital media. [Available online at https://www.fsa.usda.gov.].

[36] Mathworks, "Edge detection," 2022, digital media. [Available online at https://www.mathworks.com/help/images/edge-detection.html.].

[37] M. B. Schreck, P. J. Howerton, and K. R. Cook, "Adapting Australia's grassland fire danger index for the United States' central plains," *Central Region Technical Attachment*, no. 10-02, 2010.

[38] M. M. Valero, S. Verstockt, B. Butler, D. Jimenez, O. Rios, C. Mata, L. Queen, E. Pastor, and E. Planas, "Thermal Infrared Video Stabilization for Aerial Monitoring of Active Wildfires," *IEEE Journal of Selected Topics in Applied Earth Observations and Remote Sensing*, vol. 14, pp. 2817–2832, 2021.